European Radiology
https://doi.org/10.1007/s00330-021-07991-x

PAEDIATRIC

Radiogenomics of diffuse intrinsic pontine gliomas (DIPGs): correlation of histological and biological characteristics with multimodal MRI features

Raphaël Calmon[1,2,3] · Volodia Dangouloff-Ros[1,2,3] · Pascale Varlet[4,5] · Christophe Deroulers[6] · Cathy Philippe[7] · Marie-Anne Debily[8] · David Castel[8] · Kevin Beccaria[9,10] · Thomas Blauwblomme[9,10] · David Grevent[1,2,3] · Raphael Levy[1,2,3] · Charles-Joris Roux[1,2,3] · Yvonne Purcell[11] · Ana Saitovitch[2,3] · Monica Zilbovicius[2,3] · Christelle Dufour[8,12] · Stéphanie Puget[9,10] · Jacques Grill[8,12] · Nathalie Boddaert[1,2,3]

Received: 9 December 2020 / Revised: 10 March 2021 / Accepted: 9 April 2021

Abstract

Objectives The diffuse intrinsic pontine gliomas (DIPGs) are now defined by the type of histone H3 mutated at lysine 27. We aimed to correlate the multimodal MRI features of DIPGs, H3K27M mutant, with their histological and molecular characteristics.

Methods Twenty-seven treatment-naïve children with histopathologically confirmed DIPG H3K27M mutant were prospectively included. MRI performed prior to biopsy included multi-b-value diffusion-weighted imaging, ASL, and dynamic susceptibility contrast (DSC) perfusion imaging. The ADC and cerebral blood flow (CBF) and blood volume (CBV) were measured at the biopsy site. We assessed quantitative histological data, including microvascular density, nuclear density, and H3K27M-positive nuclear density. Gene expression profiling was also assessed in the samples. We compared imaging and histopathological data according to histone subgroup. We correlated MRI quantitative data with histological data and gene expression.

Results H3.1K27M mutated tumors showed higher ADC values (median 3151 $\mu m^2/s$ vs 1741 $\mu m^2/s$, $p = 0.003$), and lower perfusion values (DSC-rCBF median 0.71 vs 1.43, $p = 0.002$, and DSC-rCBV median 1.00 vs 1.71, $p = 0.02$) than H3.3K27M ones. They had similar microvascular and nuclear density, but lower H3K27M-positive nuclear density ($p = 0.007$). The DSC-rCBV was positively correlated to the H3K27M-positive nuclear density (rho = 0.74, $p = 0.02$). ADC values were not correlated with nuclear density nor perfusion values with microvascular density. The expression of gated channel activity–related genes tended to be inversely correlated with ADC values and positively correlated with DSC perfusion.

Conclusions H3.1K27M mutated tumors have higher ADC and lower perfusion values than H3.3K27M ones, without direct correlation with microvascular or nuclear density. This may be due to tissular edema possibly related to gated channel activity–related gene expression.

Raphaël Calmon and Volodia Dangouloff-Ros contributed equally to this work.

✉ Volodia Dangouloff-Ros
volodia.dangouloff-ros@aphp.fr

1 Pediatric Radiology Department, AP-HP, Hôpital Universitaire Necker-Enfants Malades, 149 rue de Sèvres, F-75015 Paris, France

2 Université de Paris, INSERM ERL UA10, F-75015 Paris, France

3 Université de Paris, UMR 1163, Institut Imagine, F-75015 Paris, France

4 Neuropathology Department, Sainte-Anne Hospital, F-75014 Paris, France

5 Université de Paris, INSERM U894, IMA BRAIN, F-75014 Paris, France

6 Université Paris-Saclay, CNRS/IN2P3, IJCLab, F-91405 Orsay, France

7 Université Paris-Saclay, Neurospin, Institut Joliot, CEA, Gif-sur-Yvette, France

8 Université Paris-Saclay, UMR8203, CNRS, F-94805 Villejuif, France

9 Pediatric Neurosurgery Department, AP-HP, Hôpital Universitaire Necker-Enfants Malades, F-75015 Paris, France

10 Université de Paris, F-75015 Paris, France

11 Radiology Department, Fondation Rothschild, F-75019 Paris, France

12 Department of Pediatric and Adolescent Oncology, Institut Gustave Roussy, F-94805 Villejuif, France

Published online: 18 May 2021

Key Points

- *H3.1K27M mutant DIPG had higher apparent diffusion coefficient (p = 0.003), lower α (p = 0.048), and lower relative cerebral blood volume (p = 0.02) than H3.3K27M mutant DIPG at their biopsy sites.*
- *Biopsy samples obtained within the tumor's enhancing portion showed higher microvascular density (p = 0.03) than samples obtained outside the tumor's enhancing portion, but similar H3K27M-positive nuclear density (p = 0.84).*
- *Relative cerebral blood volume measured at the biopsy site was significantly correlated with H3K27M-positive nuclear density (rho = 0.74, p = 0.02).*

Keywords Diffuse intrinsic pontine glioma · Child · Diffusion magnetic resonance imaging · Perfusion-weighted magnetic resonance imaging · Genetic association studies

Abbreviations

CBF	Cerebral blood flow
CBV	Cerebral blood volume
DIPG	Diffuse intrinsic pontine glioma
DSC	Dynamic susceptibility contrast
FLAIR	Fluid-attenuated inversion recovery
WHO	Word Health Organization

Introduction

Diffuse intrinsic pontine gliomas (DIPGs) have long been diagnosed by imaging only in the context of rapidly evolving symptoms. Recently, some teams have re-introduced stereotactic biopsies in the diagnostic work-up of these tumors [1], which, together with data obtained at autopsy by other teams [2], has prompted a more biological definition of these neoplasms. This was reflected in the 2016 update of the WHO classification [3], introducing the entity diffuse midline glioma, H3K27M mutant. It comprises all infiltrating gliomas located in the thalamus, midbrain, pons (where the tumors are called DIPG), medulla, spinal cord, and cerebellum, harboring a somatic mutation at the lysine residue 27 in one of the histone 3 genes [3, 4].

In about two-thirds of patients, the mutation affects the H3.3 variant gene (*H3F3A*) while it affects one of the H3.1 genes (*HIST1H3B* or *HIST1H3C*) in a quarter [5]. Ten percent of DIPGs do not contain these mutations but the action of the mutation is mimicked by the re-expression of an EZH interactor protein [6]. The histone variant affected by the K27M mutation is associated with specific phenotypic characteristics, since H3.1K27M patients are younger, respond better to radiotherapy, and metastasize less frequently, and consequently have a longer albeit similar evolution [4, 7, 8]. Extensive biological characterization of stereotactic biopsies has been previously described [4, 9] and proven feasible [1], supporting their use in the context of a trial and for precision medicine.

MRI is not only a non-invasive way to diagnose DIPG that remains useful for many teams who do not perform biopsies but also represents an invaluable way to monitor tumor evolution during treatment [10]. In addition, it gives a sense of tumor heterogeneity that cannot be fully appreciated with stereotactic biopsies alone. Several teams reported attempts to distinguish H3K27M mutant from H3K27M wild-type DIPG [11–15], or long-term survivors from short-term survivors [8, 15–25].

Only rare studies have tried to correlate imaging features with biologic correlates such as the type of histone H3K27M mutated [4, 26]. However, the pathophysiological mechanisms of these changes are still to be elucidated. One of the pitfalls of such analyses is the radiological heterogeneity of DIPG possibly associated with a corresponding biological heterogeneity [27]. Therefore, we postulated that correlative analyses should be focused on the biopsy site as depicted on post-operative MRI to assess the correlation between MRI and histological metrics more properly and inform our understanding of the tumor phenotypes.

The purpose of this study was then to correlate the multimodal MRI features of DIPGs, H3K27M mutant, with their histological and biological characteristics at the specific site of biopsy. We hypothesized that H3.1 and H3.3 mutant DIPGs had different multimodal MRI features and that these differences may be explained by histopathological characteristic features.

Materials and methods

Population

Consecutive treatment-naïve children presenting with clinical and radiological findings suggestive of DIPG underwent a multimodal MRI prior to stereotactic biopsy in Necker-Enfants Malades Hospital, Paris, France. After the biopsy, a control imaging study was performed to screen for complications and confirm the location sampled. If H3K27M mutation was confirmed, they were prospectively included (see Fig. 1). Nine subjects were excluded

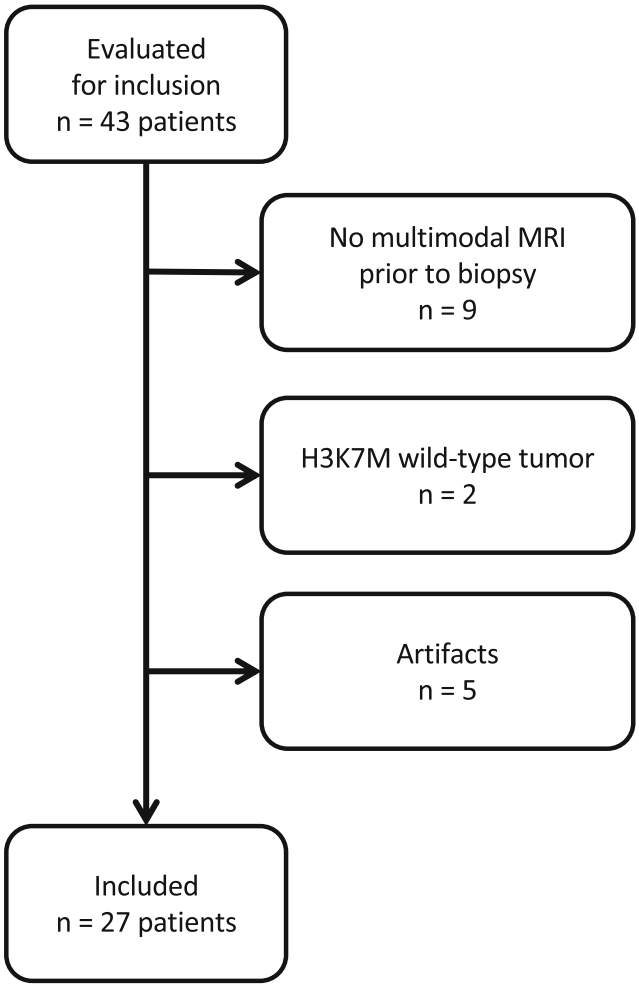

Fig. 1 Flow diagram

because they did not have multimodal MRI prior to biopsy, 2 because no H3K27M mutation was found, and 5 because motion artifacts precluded multimodal image analysis. Overall, this study included 27 children, 15 girls (median age 5.8 years, range 3.9–15.2 years) and 12 boys (median age 7.3 years, range 3.3–14.7 years). Among the 27 children included, 17 subjects had been published in a previous molecular analysis study [4].

Ethical approval was obtained from our IRB (EDRACT 2014-A-00541–46). Informed consent was obtained from the patients' families who authorized the use of biological, clinical, and radiological data recorded for research purposes.

MRI acquisition and post-processing

MR imaging was performed with a Signa HDxt 1.5-T system (GE Healthcare) and a 12-channel head-neck-spine coil. The routine MRI protocol included volumetric sequences: T2 and T2 fluid-attenuated inversion recovery (FLAIR)–weighted images and pre- and post-contrast T1-weighted images. Multimodal imaging included ASL perfusion, multi-b-value diffusion, and dynamic susceptibility contrast (DSC) perfusion imaging (parameters in Supplemental Methods).

All the MRI data were transferred to a workstation running Olea Sphere® (Olea Medical) software for post-processing. DSC perfusion data generated were as follows: cerebral blood volume (DSC-CBV) corrected for contrast leakage [28] and cerebral blood flow (DSC-CBF) maps. By applying a stretched exponential model to the multi-b-value diffusion data, ADC and water molecular diffusion heterogeneity index (α) maps were calculated. The MRI scanner generated cerebral blood flow (CBF) maps automatically from the ASL data (ASL-CBF). The MRI data was transferred to an OsiriX® workstation, and co-registration of the multimodal maps to the volumetric T1-weighted images was performed using FLIRT affine transformation (FSL Version 6.0) [29]. Post-biopsy MRI was also co-registered to the pre-biopsy T1-weighed images for each patient. Spherical volumes of interest (VOIs) of 1 cm in diameter (0.5 cm^3) were drawn over the area corresponding to the biopsy site by an experienced pediatric neuroradiologist (RC, 8 years of experience), blinded to histological and molecular data. The VOIs were transferred to the five multimodal MRI maps (ASL-CBF, DSC-CBF, DSC-CBV, ADC, and α), and the VOI's mean value was recorded. A VOI of all available, normal-appearing, supratentorial white matters on the DSC-CBF and DSC-CBV maps was created using a semi-automated segmentation tool. The white matter VOI's mean value was used as reference to calculate relative values of DSC blood flow (DSC-rCBF) and DSC blood volume (DSC-rCBV). The reference ASL-CBF value was measured at the cortex of the left cerebellar hemisphere, using the mean value of a manually drawn 50 mm^2 region of interest in the axial plane. This reference value was then used to calculate the relative ASL-CBF (ASL-rCBF). The presence of necrosis, post-contrast enhancement on T1-weighted images at the biopsy site and at any other region of the tumor was recorded.

Histological staining, scanning, and segmentation

A qualitative analysis of the samples was performed by a neuropathologist with expertise in pediatric brain tumors including DIPG (PV, 20 years of experience). Formalin-fixed paraffin-embedded tissues were subjected for routine MIB, CD34, and H3K27M immunostainings to a Ventana autostainer (BenchMark XT, Roche Diagnostics) according to published protocols [4, 30]. A quantitative analysis of stained then scanned samples was performed as previously described [30, 31]. Microvascular density was defined by the total area of vessel walls as a percentage of the entire tissue area, and nuclear density as the total area occupied by the non-

endothelial nuclei as a percentage of the entire tissue area. Nuclear density was also separately measured for MIB-positive cells and H3K27M-positive cells. Tumorous cell ratio was defined as the number of H3K27M-positive nuclei divided by the total number of nuclei. The ratio of tumorous cell cycling was the number of MIB-positive nuclei divided by the number of H3K27M-positive nuclei.

Gene expression correlation with multimodal MRI features

In a subset of 11 tumors from the 27 included in the study, whole gene expression was obtained on Agilent Microarrays as previously described [1, 4] and was used to compare differentially expressed genes in H3.1- and H3.3K27M mutated DIPG. The most differentially expressed genes in H3.1- and H3.3K27M mutated DIPG were correlated with quantitative MRI data (ADC, ASL-rCBF, DSC-rCBV, and DSC-rCBF) at the site of the stereotactic biopsy.

Statistical analysis

The results were analyzed using R Project for Statistical Computing 3.3.3 (http://www.r-project.org), using an alpha level set at 5%.

The Wilcoxon rank-sum test (with effect size r calculation) was used to compare the measured values of the multimodal MRI parameters and the histological parameters between the H3.1K27M mutant and H3.3K27M mutant lesions, and between enhancing and non-enhancing biopsy sites. Fisher's exact test was used to compare H3.1- to H3.3K27M mutant lesions regarding the presence of radiological necrosis, contrast enhancement within the lesion, and the presence of enhancement specifically at the biopsy site.

The Spearman method was used to test the correlation between quantitative histologic and molecular features and multimodal MRI quantitative data. To take into account the large number of correlation tests, the Benjamini-Hochberg procedure was used to control the false discovery rate.

Survival was estimated using the Kaplan-Meier method and group comparisons were made using log-rank test.

Results

Population

All tumors met the classical radiological (see Supplemental Figure S1) and clinical criteria of DIPG [10]. The mutation concerned the H3.3 variant in 20 patients and it affected the H3.1 canonical histone in 7. Table 1 includes the clinical symptoms and structural MRI aspects for all 27 patients. H3.1 patients were younger than H3.3 patients (median 4.6 years, range [3.3–7.5] vs 6.9 years, range [3.9–15.2], Wilcoxon test $p = 0.014$, $r = 0.48$) and had longer overall survival (median 18 months, range [9–35] vs 10 months, range [6–27], log-rank test $p = 0.022$; see Fig. 2). There was no significant difference between H3.1 and H3.3 patients in term of clinical symptoms (Fisher exact test, $p = 0.2$ to 1) or time to symptoms (Fisher exact test, $p = 0.1$).

Differences between H3.1K27M and H3.3K27M mutant DIPG

Radiological features (Fig. 3)

The biopsy sites of H3.1K27M mutant tumors showed different MR diffusion parameters than those of H3.3K27M mutant tumors: H3.1 had higher ADC values (median 3151 $\mu m^2/s$, IQR [2273–3727] vs 1741 $\mu m^2/s$, IQR [1282–1944], Wilcoxon test $p = 0.003$, $r = 0.54$) and lower α (median 0.53, IQR [0.49–0.53] vs 0.59, IQR [0.54–0.63], Wilcoxon test $p = 0.08$, $r = 0.38$).

Perfusion parameters using DSC were lower in H3.1K27M mutant tumors, with lower DSC-rCBF (median 0.71, IQR [0.44–0.79] vs 1.43, IQR [1.03–2.08], Wilcoxon test $p = 0.002$, $r = 0.56$) and lower DSC-rCBV (median 1.00, IQR [0.68–1.14] vs 1.71, IQR [1.31–1.95], Wilcoxon test $p = 0.02$, 0.44). ASL measurements did not significantly differ between the two groups (ASL-rCBF median 0.67, IQR [0.56–0.70] vs 0.70, IQR [0.58–0.79], Wilcoxon test $p = 0.24$, $r = 0.24$).

Contrast enhancement was slightly more frequent in H3.1K27M mutant lesions, yet not significantly, in the biopsy site (57% (4/7) vs 25% (5/20); Fisher exact test $p = 0.18$), nor within the whole tumor (86% (6/7) vs 65% (13/20); Fisher exact test $p = 0.63$). The results were similar in terms of the presence of necrosis (71% (5/7) vs 60% (12/20); Fisher exact test $p = 0.68$).

Histological features

All samples displayed usual DIPG qualitative features.

Samples from H3.1- and H3.3K27M mutant lesions had similar nuclear density and microvascular density.

H3.3K27M mutant tumors had higher H3K27M-positive nuclei density (Wilcoxon test $p = 0.007$, $r = 0.60$) and higher tumor cell ratio (Wilcoxon test $p = 0.005$, $r = 0.62$). There was a trend for H3.3K27M mutant tumors to have lower MIB-1-positive nuclear density (Wilcoxon test $p = 0.08$, 0.34). These opposite results resulted in a lower ratio of tumorous nuclei cell cycling (Wilcoxon test $p = 0.01$, $r = 0.58$) in H3.3K27M mutant tumors.

Table 1 Clinical and structural MRI data of the 27 patients

	Sex	Age (years)	H3K27M mutation status	Time from onset of symptoms (months)	Overall survival (months)	Cranial nerve deficit	Ataxia	Long tract signs	Lesion enhancement	Biopsy site enhancement	Necrosis
1	M	3.3	1	4	27	III	Yes	Hemiplegia	Yes	Yes	Yes
2	M	3.7	1	1	9	None	No	Monoplegia	Yes	Yes	Yes
3	F	4.4	1	0.75	17	III, VI	No	None	No	No	None
4	M	4.6	1	1	10	III	No	Hemiparesis	Yes	Yes	Yes
5	F	5.2	1	3	18	VI	Yes	Pyramidal signs	Yes	No	Minimal
6	F	5.8	1	0.5	26	None	Yes	Hemiplegia	Yes	Yes	Yes
7	M	7.5	1	0.75	35	VII	Yes	Hemiparesis	Yes	No	None
8	F	3.9	3	0.75	13	VI	Yes	Hemiparesis	Yes	Yes	Yes
9	F	4.1	3	0.75	9	None	Yes	None	No	No	None
10	F	4.8	3	1	10	VI, IX	No	Pyramidal signs	Yes	No	Yes
11	F	5.1	3	0.5	6	III, VI	No	None	Yes	Yes	Yes
12	F	5.7	3	0.75	13	VI, VII	Yes	Hemiparesis	Yes	No	Minimal
13	M	5.7	3	1	11	VII	Yes	Hemiparesis	Yes	Yes	Yes
14	M	5.9	3	3	10	IX, IV	Yes	Pyramidal signs	Yes	No	Minimal
15	F	6.2	3	0.75	10	IV	No	None	No	No	None
16	F	6.7	3	0.5	7	IX	Yes	Diplegia	Yes	Yes	Minimal
17	F	6.7	3	1	27	VI, VII	Yes	None	No	No	None
18	M	7.1	3	1	9	VI	Yes	None	Yes	Yes	Yes
19	F	7.8	3	0.2	8	VI	No	None	No	No	None
20	F	8	3	2	10	VI	Yes	Pyramidal signs	Yes	No	Minimal
21	M	9.3	3	1	22	VI	No	Pyramidal signs	No	No	None
22	M	9.4	3	1.2	8	VI	No	Pyramidal signs	Yes	No	Minimal
23	F	9.7	3	1.75	12	VI, VII	No	None	No	No	None
24	M	12.3	3	2	8	III, V, VI	Yes	None	Yes	No	None
25	M	14	3	0.2	10	VI, VII	Yes	Pyramidal signs	Yes	No	Minimal
26	M	14.7	3	1	15	IX, VI	Yes	Pyramidal signs	No	No	None
27	F	15.2	3	1	20	VI, VII	No	None	Yes	No	Yes

Differences according to the presence of enhancement at the biopsy site (Fig. 4)

Overall survival was similar between patients demonstrating contrast enhancement or not.

The measured multimodal MRI quantitative parameters (ADC, α, ASL-rCBF, DSC-rCBV, and DSC-rCBF) did not differ significantly between enhancing and non-enhancing biopsy sites.

Biopsy samples obtained within the tumor's enhancing portion showed higher microvascular density than samples obtained outside the tumor's enhancing portion (Wilcoxon test $p = 0.03$, $r = 0.42$). They also had higher nuclear density (Wilcoxon test $p = 0.03$, $r = 0.43$), higher MIB-positive nuclear density (Wilcoxon test $p = 0.04$, $r = 0.39$), and higher ratio of tumorous cell cycling (Wilcoxon test $p = 0.02$, $r = 0.52$). However, there was no significant difference in H3K27M-positive nuclear density or tumorous cell ratio.

Correlation between histological and multimodal MRI quantitative data

There was a significant positive correlation between the rCBV measured at the biopsy sites and H3K27M-positive nuclear density measured in the tumor samples (Spearman rho = 0.74, $p < 0.001$, corrected to 0.02) (Fig. 5). There were weaker correlations between rCBF and H3K27M-positive nuclear density (Spearman rho = 0.53, $p = 0.02$, corrected to 0.36) and between rCBV and nuclear density (Spearman rho = 0.40, $p = 0.04$, corrected to 0.45).

No other significant correlation was found; noticeably, there was no correlation between ADC and tumor cell content, nor between microvascular density and perfusion values.

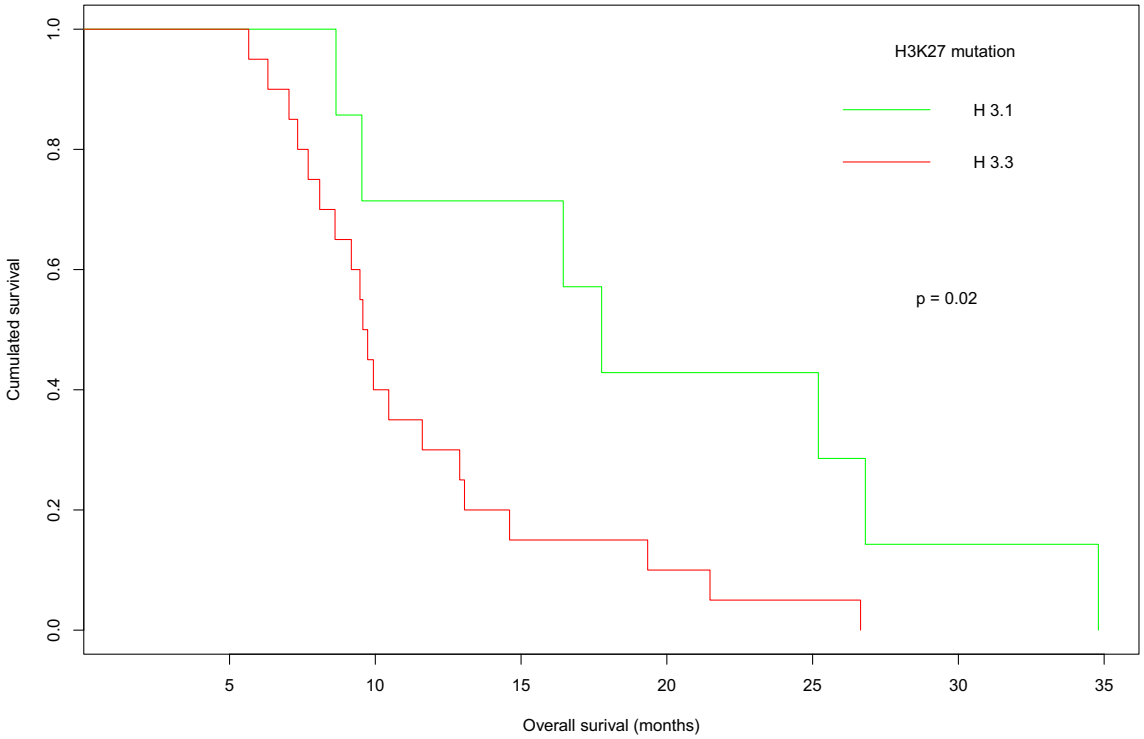

Fig. 2 Overall survival differences in subjects with H3.1K27M ($n = 7$) versus H3.3K27M ($n = 20$) tumors. Patients with H3.1K27M mutant tumors had significantly longer overall survival ($p = 0.022$) than patients with H3.3K27M mutant tumors

Correlation between gene expression and multimodal MRI quantitative data

The 3 molecular function categories with the highest expression difference between H3.1- and H3.3K27M mutant lesions appeared to be linked to gated channel activity–related genes. Fourteen out of the 18 top genes up-regulated in H3.3K27M tumors compared to H3.1K27M tumors were ion channels. Most of these genes were inversely correlated with ADC values and positively correlated with α and DSC perfusion values (DSC-rCBV, DSC-rCBF) (Table 2). No consistent correlation was found using ASL. However, due to the small number of samples tested, these gene expression-MRI metrics correlations were not statistically significant after correction for multiple comparisons.

Discussion

We report different multimodal imaging characteristics at the biopsy site between H3.1 and H3.3 mutated DIPG, and correlated it with histological data. Compared to H3.1K27M mutant DIPG, biopsy sites of the H3.3K27M variant displayed lower ADC, higher α, and higher DSC-rCBV and DSC-rCBF. Histopathologically, H3.3K27M mutant tumors had higher H3K27M-positive nuclei density and higher tumorous cell ratio. We found a positive correlation between the rCBV measured at the biopsy sites and H3K27M–positive nuclear density measured in the tumor samples.

Consistent with previous reports [4, 26], we observed that H3.1- versus H3.3K27M mutations were strong prognostic markers, with better overall survival, and that H3.1K27M mutated DIPGs occur at a younger age. To date, the DIPG imaging literature mainly contains reports comparing H3K27 mutant and H3K27 wild-type DIPG [11–15], or long-term versus short-term survivors [8, 15–17, 19, 22, 24], but only a few studies explore imaging characteristics according to histone mutation [4, 26].

As reported in other studies [4, 26], contrast enhancement at the biopsy site and in the whole tumor tends to be more frequent in H3.1 mutated tumors. Castel et al [4] and Jaimes et al [26] also reported non-significant differences in terms of enhancement presence, but more striking differences when studying enhancement volume or large necrotic areas with ring enhancement. The presence of contrast enhancement at the biopsy site was associated with higher values of microvascular density, consistent with gadolinium-chelate contrast agent leakage through a disrupted blood–brain barrier, commonly observed in newly formed vessels derived from tumor-induced angiogenesis [32]. It is concordant with the enrichment of neo-angiogenic genes in H3.1 mutated DIPG and their hypoxia signature [4], inducing tumoral angiogenesis with abnormal blood–brain barrier. Several studies reported an association between contrast enhancement and shorter overall survival without taking into account histone mutation [8, 19, 22, 23, 25, 26], which may

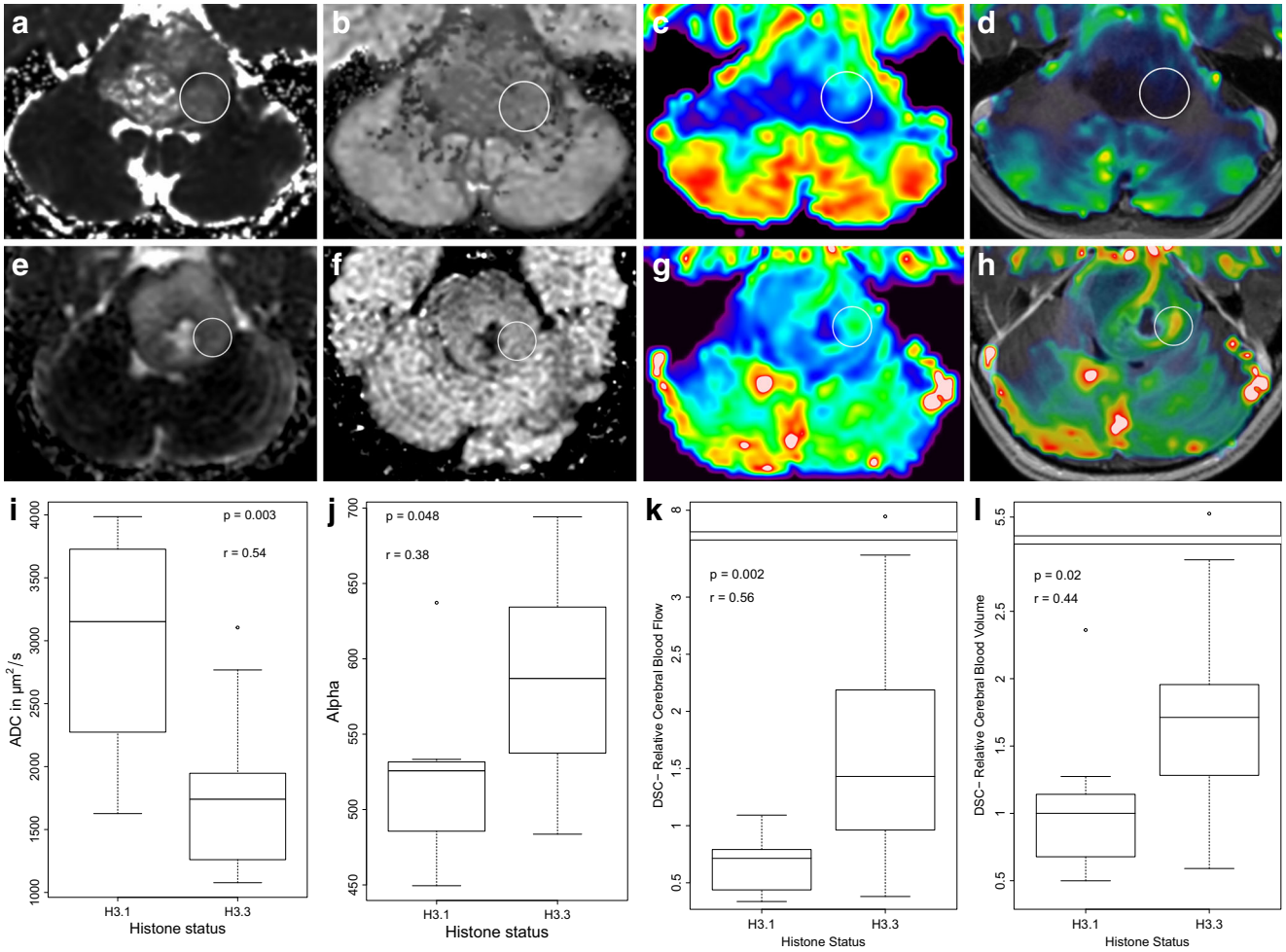

Fig. 3 Radiological differences between H3.1 and H3.3 mutant tumors. Examples of H3.1 (top row) and H3.3 (bottom row) mutated DIPG: ADC (**a**, **e**), water molecular diffusion heterogeneity index (α) (**b**, **f**), dynamic susceptibility contrast (DSC) relative cerebral blood flow (rCBF) (**c**, **g**), and DSC relative cerebral blood volume (rCBV) map over contrast-enhanced T1-weighted image (**d**, **h**). Boxplot with whiskers representing the distribution of ADC (**i**), α (**j**), DSC-rCBF (**k**), and DSC-rCBV (**l**) values at the biopsy sites (identified by a white ROI) according to histone H3 mutation status, with p value and r value of Wilcoxon tests. H3.1 tumors had significantly higher ADC values ($p = 0.003$) and lower α ($p = 0.048$), DSC-rCBF ($p = 0.002$), and DSC-rCBV ($p = 0.02$) values

appear confusing if H3.1 tumors with better prognosis have more pronounced enhancement. Jaimes et al [26] found that the presence of enhancement was significantly associated with shorter overall survival, and that the tumoral volume enhancing had a strong trend towards reduced progression-free survival, while in the same cohort, H3.1 tumors had higher tumoral volume enhancing. This highlights the multifactorial approach needed to predict survival of these patients, and leads further larger studies to assess prognostic value of radiological features in each molecular subgroup. To date, histone mutation has been reported as a stronger prognostic factor than clinico-radiological evaluation including contrast enhancement [4].

We found that ADC values were lower in biopsy sites of H3.3 tumors than in those of H3.1 tumors. Studying the whole tumor, Jaimes et al [26] found such a difference of median ADC and mode ADC, but Castel et al [4] found a different distribution of ADC values in the whole tumor which tend to be lower in H3.1 tumors. This reflects the radiological heterogeneity within these tumors, since we studied only the biopsy site while previous reports analyzed the entire tumor minus the necrotic area. Jaimes et al [26] also reported higher skewness and kurtosis in H3.3 tumors, hypothesizing that it may reflect higher cellularity in H3.3 tumors. However, interpretation of ADC differences in our cohort seemed to be different from adult gliomas, not relying on tumor cellularity, but may be on edema. Indeed, ADC was not correlated with tumor cell content in our samples, but was associated (yet not significantly) with ion channel gene depletion, which may increase edema. α was lower in H3.1 tumors, which reflects higher tissue heterogeneity. This may also be linked to higher edema in H3.1 tumors because of ion channel gene downregulation. Indeed, for example, loss of CACNA1A activity in CACNA1A encephalopathy is associated with extreme brain edema [33]. Further functional studies are needed to establish formally this link, however. ADC variations in

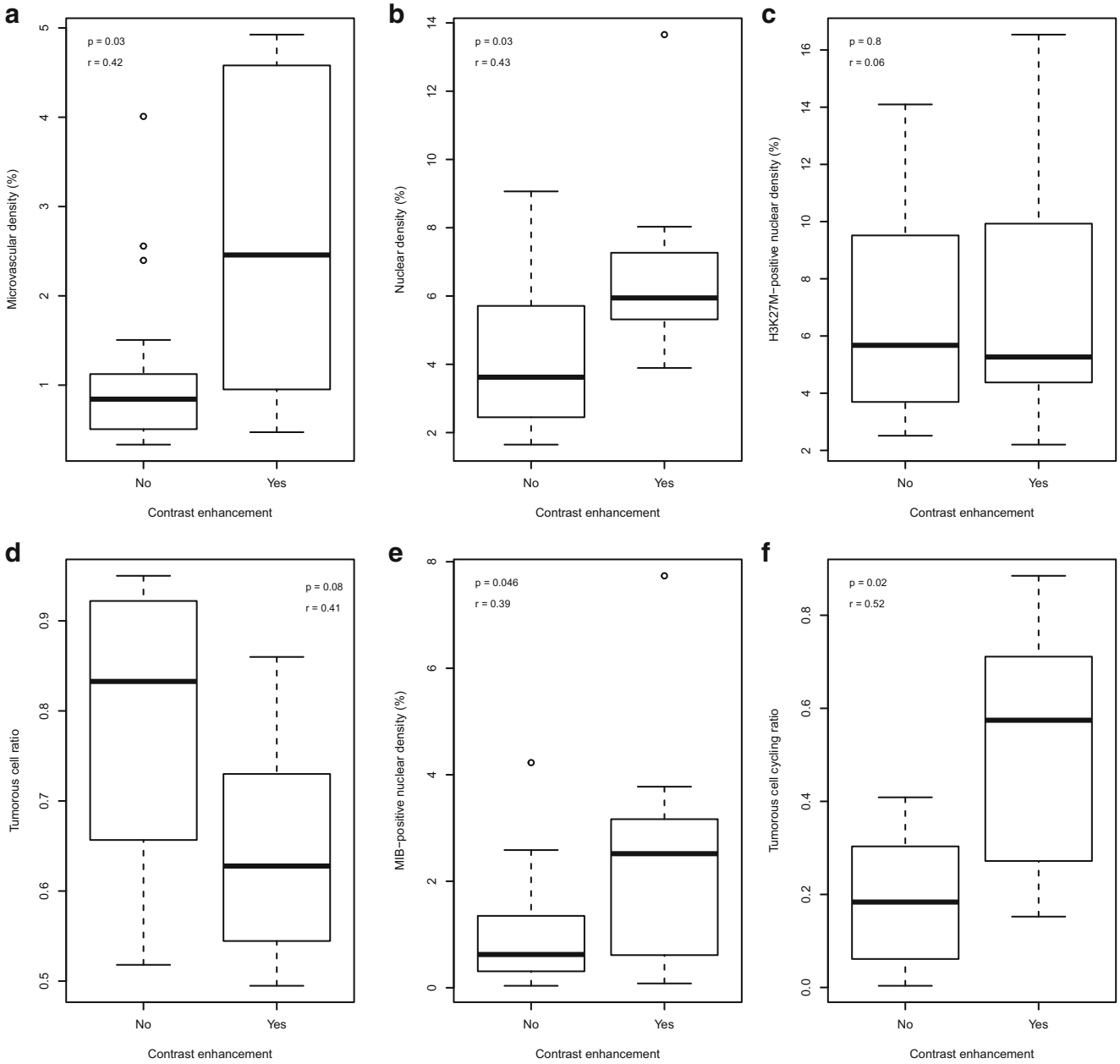

Fig. 4 Histological differences between enhancing and non-enhancing biopsy sites. Boxplot with whiskers showing the distribution of microvascular density (**a**), nuclear density (**b**), H3K27M-positive nuclear density (**c**), tumorous cell ratio (**d**), MIB-positive nuclear density (**e**), and tumorous cell cycling ratio (**f**) values at the biopsy sites according to the presence or absence of enhancement, with p value and r value of Wilcoxon tests. Enhancing biopsy sites presented higher microvascular density ($p = 0.03$), nuclear density ($p = 0.03$), MIB-positive nuclear density ($p = 0.04$), and ratio of tumorous cell cycling ($p = 0.02$). The H3K27M-positive nuclear density and the ratio of tumorous cell in the tissue did not significantly differ between samples from enhancing and non-enhancing sites ($p = 0.84$ and $p = 0.08$, respectively)

DIPG are more likely multifactorial, and larger MRI-histopathology studies would help to elucidate the pathophysiological mechanisms involved.

Using DSC PWI, rCBV and rCBF were higher in the biopsy site of H3.3 tumors. rCBV was significantly correlated with H3K27M-positive nuclear density measured in the tumor samples, but not correlated with microvascular density. Furthermore, the microvascular density was not significantly different between H3.1 and H3.3 groups. As suggested by the poor vasculature reported in mice xenografts [34], these differences are seen between two groups of hypoperfused tumors. We may hypothesize that higher edema in H3.1 tumors could be responsible for the lower rCBV and rCBF indexes. Indeed, in tissues with limited capacity to expand, such as the brainstem, increase in extracellular volume will cause an increase in interstitial fluid pressure, leading to a reduced vascular transmural pressure gradient and physical compression of the capillaries [35]. The

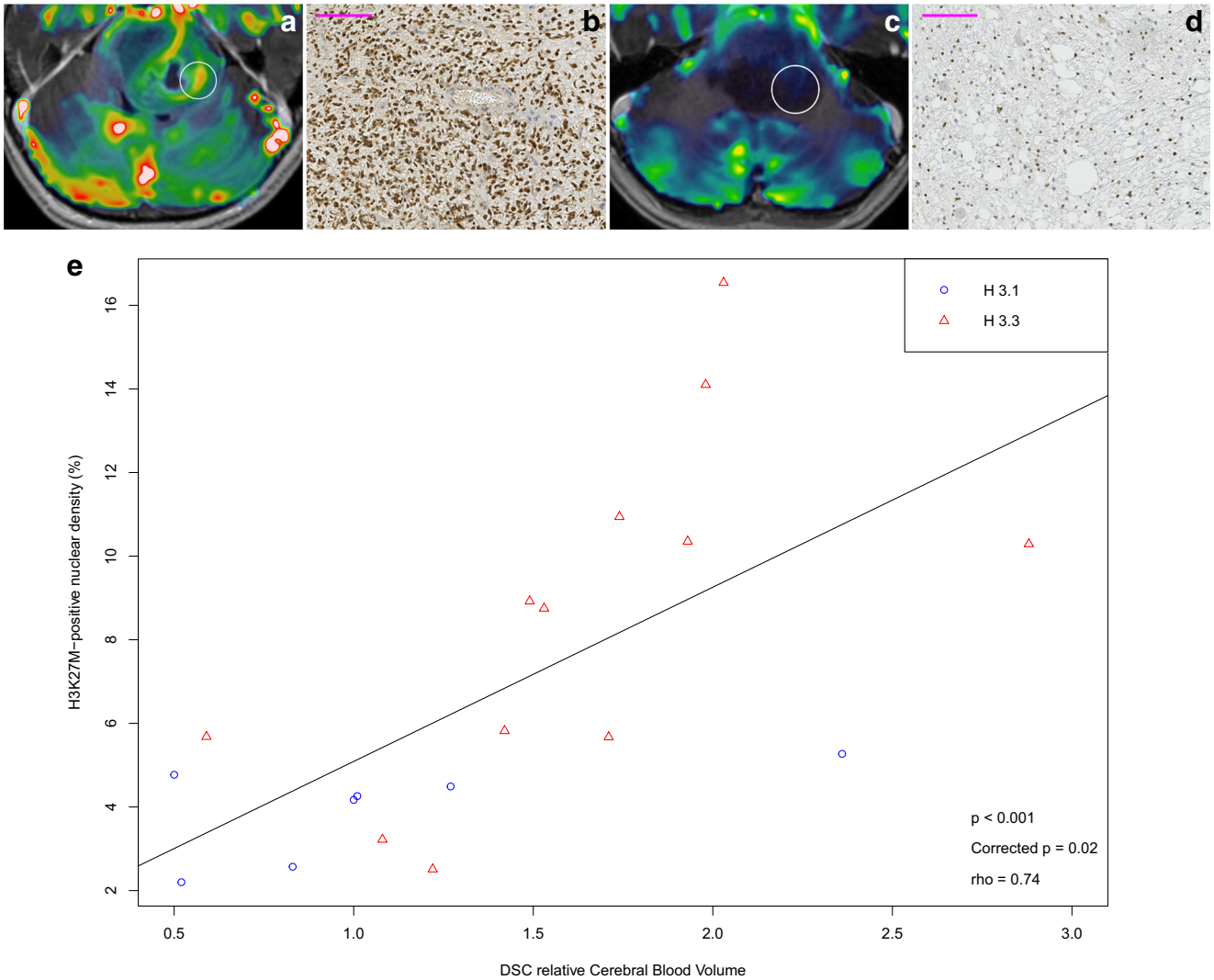

Fig. 5 Correlation between H3K27M-positive nuclear density and relative cerebral blood volume. Dynamic susceptibility contrast (DSC) relative cerebral blood volume (rCBV) map over contrast-enhanced T1-weighted image (**a**, **c**) with the biopsy site marked by a white target and the corresponding H3K27M-stained biopsy samples (**b**, **d**). High DSC-rCBV biopsy site (top row) shows high H3K27M+ nuclear density and qualitatively no edema. Low DSC-rCBV biopsy site (bottom row) shows low H3K27M+ nuclear density and abundant edema seen as clear vacuoles. Scatter plot (**e**) of the correlation between H3K27M-positive nuclear density and DSC-rCBV measured at the biopsy site. Spearman's rank correlation rho = 0.74, $p = 0.02$ after correction for multiple comparisons. Blue circles represent measurements from H3.1 lesions and red triangles from H3.3 lesions. The black line represents the data's linear regression

same mechanism could explain the increased blood flow and blood volume observed following radiation therapy [36, 37], when edema decreases with concurrent decrease in ADC values [17, 19, 37]. Conversely, this edema-induced hypoperfusion may explain the hypoxia and neoangiogenesis in H3.1 tumors. However, several factors probably come into play to explain DSC PWI differences, mixing edema, angiogenesis, and tumor metabolism.

ASL PWI had different results than DSC PWI, since ASL-rCBF was similar between H3.1 and H3.3 tumors. Morana et al found a correlation between ASL and DSC data in pediatric astrocytic tumors [38], whereas Dangouloff-Ros et al found discordant results in choroid plexus tumors [39]. This highlights the different pathophysiological mechanisms involved with this two PWI techniques. Using freely diffusible tracer (marked water protons) in contrast with intravascular gadolinium-based contrast media, ASL PWI may be less influenced by capillary pressure.

H3.1 and H3.3 mutant tumors had the same nuclear density, but H3.3 tumors had a higher H3K27M-positive nuclear density. The H3K27M-positive nuclear density was not different between samples from enhancing and non-enhancing areas. This supports the hypothesis that the biopsy does not need to target the tumor's enhancing component to yield diagnostic information. rCBV was significantly correlated with H3K27M-positive nuclear density. However, choosing the high rCBV areas as biopsy targets to maximize the

Table 2 Spearman rank correlation coefficients between gene expression and multimodal MRI quantitative data (n = 11 patients)

		Diffusion data		Perfusion data		
Rho		ADC	α	rASL-CBF	rDSC-CBF	rDSC-CBV
Calcium channel	*CACNA1A*	− 0.38	0.24	0.09	0.54	0.61
	CACNA1B	− 0.30	− 0.07	− 0.27	0.20	0.09
	CACNA1E	0.10	0.16	− 0.39	− 0.03	0.25
	CACNG1	0.03	0.16	0.22	0.31	0.12
	TRPC3	− 0.42	0.73*	0.10	0.68*	0.39
	TRPC5	− 0.27	0.31	0.05	0.59	0.28
Potassium channel	*KCNA3*	− 0.64*	0.47	0.05	0.68*	0.35
	KCNG3	− 0.22	0.27	0.10	0.14	− 0.01
	KCNH2	− 0.84*	0.30	0.21	0.65*	0.15
	KCNH3	− 0.31	− 0.08	− 0.01	− 0.07	− 0.41
	KCNMB2	0.07	0.18	− 0.59	0.19	0.50
Na channel	*ASIC1*	− 0.67*	0.45	0.15	0.70*	0.26
Glu channel	*GRIK3*	− 0.04	0.54	0.26	0.76*	0.58
Ion channel	*CNGA3*	− 0.12	− 0.32	− 0.15	0.35	0.50

Most of the channel-related genes are inversely correlated with ADC values and positively correlated with α and DSC perfusion values (DSC-rCBV, DSC-rCBF). No consistent correlation was found using ASL. *Indicates a p value below 0.05 before correction for multiple comparisons. No correlation remains statistically significant after correction for multiple comparisons. Gene names match NCBI gene denomination. *DSC* dynamic susceptibility contrast, *CBF* cerebral blood flow, *CBV* cerebral blood volume

opportunity to detect H3K27M mutant cells may be not relevant, as biopsy site choice should primarily minimize the surgical risk, without jeopardizing good diagnostic performance [1].

This study has several limitations. First, we report a small number of patients because of the prospective single-center design of our study. This precludes subgroups analyses and supports further larger studies to assess performance of the radiological features to predict molecular groups and prognosis. Ideally, serial stereotactic biopsies should be performed at each of the different imaging components of the lesions. However, due to the sensitive nature of the brainstem sampling, multiple locations would result in an unreasonable risk for patients. We were unable to perform reliable quantification of edema, which would have been very useful to test the hypothetic correlation between edema and ADC or perfusion values. Another bias could result from the fact that the H3K27M antibody has a higher affinity for the histone 3.3 variant, which may induce bias when measuring the nuclear density. The nuclei of H3.3 cells were indeed darker than of H3.1 cells; however, the segmentation algorithm was adapted to account for the color difference and reduce the potential heterogeneity in nuclear density measures. More recent H3K27M antibodies may also reduce this difference.

In conclusion, the diffusion and perfusion differences that we found between H3.1- and H3.3K27M DIPG are not linked with cellular or microvascular density, but instead may be mainly explained by interstitial edema differences through different gene expressions. Physiologic mechanisms, including ion gated channel downregulation in H3.1K27M tumors, have still to be elucidated.

Supplementary Information The online version contains supplementary material available at https://doi.org/10.1007/s00330-021-07991-x.

Funding The authors state that this work has not received any funding.

Declarations

Guarantor The scientific guarantor of this publication is Nathalie Boddaert.

Conflict of interest The authors of this manuscript declare no relationships with any companies, whose products or services may be related to the subject matter of the article.

Statistics and biometry One of the authors has significant statistical expertise.

Informed consent Written informed consent was obtained from all subjects (patients) in this study.

Ethical approval Institutional Review Board approval was obtained.

Study subjects or cohorts overlap Some study subjects (17/27) or cohorts have been previously reported in a molecular analysis study (Castel et al Acta Neuropathol 2015).

Methodology
- prospective
- observational
- performed at one institution

References

1. Puget S, Beccaria K, Blauwblomme T et al (2015) Biopsy in a series of 130 pediatric diffuse intrinsic pontine gliomas. Childs Nerv Syst 31:1773–1780. https://doi.org/10.1007/s00381-015-2832-1
2. Wu G, Diaz AK, Paugh BS et al (2014) The genomic landscape of diffuse intrinsic pontine glioma and pediatric non-brainstem high-grade glioma. Nat Genet 46:444–450. https://doi.org/10.1038/ng.2938
3. Louis DN, Perry A, Reifenberger G et al (2016) The 2016 World Health Organization Classification of Tumors of the Central Nervous System: a summary. Acta Neuropathol 131:803–820. https://doi.org/10.1007/s00401-016-1545-1
4. Castel D, Philippe C, Calmon R et al (2015) Histone H3F3A and HIST1H3B K27M mutations define two subgroups of diffuse intrinsic pontine gliomas with different prognosis and phenotypes. Acta Neuropathol 130:815–827. https://doi.org/10.1007/s00401-015-1478-0
5. Lapin DH, Tsoli M, Ziegler DS (2017) Genomic insights into diffuse intrinsic pontine glioma. Front Oncol 7:57. https://doi.org/10.3389/fonc.2017.00057
6. Castel D, Kergrohen T, Tauziède-Espariat A et al (2020) Histone H3 wild-type DIPG/DMG overexpressing EZHIP extend the spectrum diffuse midline gliomas with PRC2 inhibition beyond H3-K27M mutation. Acta Neuropathol 139:1109–1113. https://doi.org/10.1007/s00401-020-02142-w
7. Castel D, Grill J, Debily M-A (2016) Histone H3 genotyping refines clinico-radiological diagnostic and prognostic criteria in DIPG. Acta Neuropathol 131:795–796. https://doi.org/10.1007/s00401-016-1568-7
8. Hoffman LM, Veldhuijzen van Zanten SEM, Colditz N et al (2018) Clinical, radiologic, pathologic, and molecular characteristics of long-term survivors of diffuse intrinsic pontine glioma (DIPG): a collaborative report from the International and European Society for Pediatric Oncology DIPG Registries. J Clin Oncol 36:1963–1972. https://doi.org/10.1200/JCO.2017.75.9308
9. Taylor KR, Vinci M, Bullock AN, Jones C (2014) ACVR1 mutations in DIPG: lessons learned from FOP. Cancer Res 74:4565–4570. https://doi.org/10.1158/0008-5472.CAN-14-1298
10. Cohen KJ, Jabado N, Grill J (2017) Diffuse intrinsic pontine gliomas-current management and new biologic insights. Is there a glimmer of hope? Neuro Oncol 19:1025–1034. https://doi.org/10.1093/neuonc/nox021
11. Piccardo A, Tortora D, Mascelli S et al (2019) Advanced MR imaging and 18F-DOPA PET characteristics of H3K27M-mutant and wild-type pediatric diffuse midline gliomas. Eur J Nucl Med Mol Imaging 46:1685–1694. https://doi.org/10.1007/s00259-019-04333-4
12. Pan C, Liu J, Tang J et al (2019) A machine learning-based prediction model of H3K27M mutations in brainstem gliomas using conventional MRI and clinical features. Radiother Oncol 130:172–179. https://doi.org/10.1016/j.radonc.2018.07.011
13. Su X, Chen N, Sun H et al (2020) Automated machine learning based on radiomics features predicts H3 K27M mutation in midline gliomas of the brain. Neuro Oncol 22:393–401. https://doi.org/10.1093/neuonc/noz184
14. Chen H, Hu W, He H et al (2019) Noninvasive assessment of H3 K27M mutational status in diffuse midline gliomas by using apparent diffusion coefficient measurements. Eur J Radiol 114:152–159. https://doi.org/10.1016/j.ejrad.2019.03.006
15. Aboian MS, Tong E, Solomon DA et al (2019) Diffusion characteristics of pediatric diffuse midline gliomas with histone H3-K27M mutation using apparent diffusion coefficient histogram analysis. AJNR Am J Neuroradiol 40:1804–1810. https://doi.org/10.3174/ajnr.A6302
16. Hargrave D, Chuang N, Bouffet E (2008) Conventional MRI cannot predict survival in childhood diffuse intrinsic pontine glioma. J Neurooncol 86:313–319. https://doi.org/10.1007/s11060-007-9473-5
17. Chen HJ, Panigrahy A, Dhall G et al (2010) Apparent diffusion and fractional anisotropy of diffuse intrinsic brain stem gliomas. AJNR Am J Neuroradiol 31:1879–1885. https://doi.org/10.3174/ajnr.A2179
18. Hipp SJ, Steffen-Smith E, Hammoud D et al (2011) Predicting outcome of children with diffuse intrinsic pontine gliomas using multiparametric imaging. Neuro Oncol 13:904–909. https://doi.org/10.1093/neuonc/nor076
19. Poussaint TY, Kocak M, Vajapeyam S et al (2011) MRI as a central component of clinical trials analysis in brainstem glioma: a report from the Pediatric Brain Tumor Consortium (PBTC). Neuro-oncology 13:417–427. https://doi.org/10.1093/neuonc/noq200
20. Lober RM, Cho Y-J, Tang Y et al (2014) Diffusion-weighted MRI derived apparent diffusion coefficient identifies prognostically distinct subgroups of pediatric diffuse intrinsic pontine glioma. J Neurooncol 117:175–182. https://doi.org/10.1007/s11060-014-1375-8
21. Conway AE, Reddick WE, Li Y et al (2014) "Occult" post-contrast signal enhancement in pediatric diffuse intrinsic pontine glioma is the MRI marker of angiogenesis? Neuroradiology 56:405–412. https://doi.org/10.1007/s00234-014-1348-9
22. Jansen MH, Veldhuijzen van Zanten SE, Sanchez Aliaga E et al (2015) Survival prediction model of children with diffuse intrinsic pontine glioma based on clinical and radiological criteria. Neuro-oncology 17:160–166. https://doi.org/10.1093/neuonc/nou104
23. Poussaint TY, Vajapeyam S, Ricci KI et al (2016) Apparent diffusion coefficient histogram metrics correlate with survival in diffuse intrinsic pontine glioma: a report from the Pediatric Brain Tumor Consortium. Neuro Oncol 18:725–734. https://doi.org/10.1093/neuonc/nov256
24. Szychot E, Youssef A, Ganeshan B et al (2020) Predicting outcome in childhood diffuse midline gliomas using magnetic resonance imaging based texture analysis. J Neuroradiol. https://doi.org/10.1016/j.neurad.2020.02.005
25. Vajapeyam S, Brown D, Billups C et al (2020) Advanced ADC histogram, perfusion, and permeability metrics show an association with survival and pseudoprogression in newly diagnosed diffuse intrinsic pontine glioma: a report from the Pediatric Brain Tumor Consortium. AJNR Am J Neuroradiol 41. https://doi.org/10.3174/ajnr.A6499
26. Jaimes C, Vajapeyam S, Brown D et al (2020) MR imaging correlates for molecular and mutational analyses in children with diffuse intrinsic pontine glioma. AJNR Am J Neuroradiol 41. https://doi.org/10.3174/ajnr.A6546
27. Harward S, Harrison Farber S, Malinzak M et al (2018) T2-weighted images are superior to other MR image types for the determination of diffuse intrinsic pontine glioma intratumoral heterogeneity. Childs Nerv Syst 34:449–455. https://doi.org/10.1007/s00381-017-3659-8
28. Harris RJ, Cloughesy TF, Hardy AJ et al (2015) MRI perfusion measurements calculated using advanced deconvolution techniques

predict survival in recurrent glioblastoma treated with bevacizumab. J Neurooncol 122:497–505. https://doi.org/10.1007/s11060-015-1755-8
29. Jenkinson M, Bannister P, Brady M, Smith S (2002) Improved optimization for the robust and accurate linear registration and motion correction of brain images. Neuroimage 17:825–841. https://doi.org/10.1016/s1053-8119(02)91132-8
30. Dangouloff-Ros V, Deroulers C, Foissac F et al (2016) Arterial spin labeling to predict brain tumor grading in children: correlations between histopathologic vascular density and perfusion MR imaging. Radiology 281:553–566. https://doi.org/10.1148/radiol.2016152228
31. Deroulers C, Dangouloff-Ros V, Badoual M et al (2016) Automatic quantification of the microvascular density on whole slide images, applied to paediatric brain tumours. Diagn Pathol 2. https://doi.org/10.17629/www.diagnosticpathology.eu-2016-2:209
32. Farnsworth RH, Lackmann M, Achen MG, Stacker SA (2014) Vascular remodeling in cancer. Oncogene 33:3496–3505. https://doi.org/10.1038/onc.2013.304
33. Camia F, Pisciotta L, Morana G et al (2017) Combined early treatment in hemiplegic attacks related to CACNA1A encephalopathy with brain oedema: blocking the cascade? Cephalalgia 37:1202–1206. https://doi.org/10.1177/0333102416668655
34. Plessier A, Le Dret L, Varlet P et al (2017) New in vivo avatars of diffuse intrinsic pontine gliomas (DIPG) from stereotactic biopsies performed at diagnosis. Oncotarget 8:52543–52559. https://doi.org/10.18632/oncotarget.15002
35. Scallan J, Huxley VH, Korthuis RJ (2010) Capillary fluid exchange: regulation, functions, and pathology. In: Colloquium lectures on integrated systems physiology: from molecules to function. Morgan & Claypool Publishers, pp 1–94
36. Sedlacik J, Winchell A, Kocak M et al (2013) MR imaging assessment of tumor perfusion and 3D segmented volume at baseline, during treatment, and at tumor progression in children with newly diagnosed diffuse intrinsic pontine glioma. AJNR Am J Neuroradiol 34:1450–1455. https://doi.org/10.3174/ajnr.A3421
37. Calmon R, Puget S, Varlet P et al (2017) Multimodal magnetic resonance imaging of treatment-induced changes to diffuse infiltrating pontine gliomas in children and correlation to patient progression-free survival. Int J Radiat Oncol Biol Phys 99:476–485. https://doi.org/10.1016/j.ijrobp.2017.04.007
38. Morana G, Tortora D, Staglianò S et al (2018) Pediatric astrocytic tumor grading: comparison between arterial spin labeling and dynamic susceptibility contrast MRI perfusion. Neuroradiology 60:437–446. https://doi.org/10.1007/s00234-018-1992-6
39. Dangouloff-Ros V, Grevent D, Pagès M et al (2015) Choroid plexus neoplasms: toward a distinction between carcinoma and papilloma using arterial spin-labeling. AJNR Am J Neuroradiol 36:1786–1790. https://doi.org/10.3174/ajnr.A4332